Journal of Materials Chemistry A

ROYAL SOCIETY OF CHEMISTRY

PAPER

View Article Online
View Journal | View Issue

Cite this: J. Mater. Chem. A, 2023, 11, 16115

Towards low-temperature processing of efficient γ-$CsPbI_3$ perovskite solar cells†

Zongbao Zhang,[ab] Ran Ji,[ab] Yvonne J. Hofstetter,[ab] Marielle Deconinck,[ab] Julius Brunner,[ab] Yanxiu Li,[ab] Qingzhi An[ab] and Yana Vaynzof *[ab]

Inorganic cesium lead iodide ($CsPbI_3$) perovskite solar cells (PSCs) have attracted enormous attention due to their excellent thermal stability and optical bandgap (~1.73 eV), well-suited for tandem device applications. However, achieving high-performance photovoltaic devices processed at low temperatures is still challenging. Here we reported a new method for the fabrication of high-efficiency and stable γ-$CsPbI_3$ PSCs at lower temperatures than was previously possible by introducing the long-chain organic cation salt ethane-1,2-diammonium iodide ($EDAI_2$) and regulating the content of lead acetate ($Pb(OAc)_2$) in the perovskite precursor solution. We find that $EDAI_2$ acts as an intermediate that can promote the formation of γ-$CsPbI_3$, while excess $Pb(OAc)_2$ can further stabilize the γ-phase of $CsPbI_3$ perovskite. Consequently, improved crystallinity and morphology and reduced carrier recombination are observed in the $CsPbI_3$ films fabricated by the new method. By optimizing the hole transport layer of $CsPbI_3$ inverted architecture solar cells, we demonstrate efficiencies of up to 16.6%, surpassing previous reports examining γ-$CsPbI_3$ in inverted PSCs. Notably, the encapsulated solar cells maintain 97% of their initial efficiency at room temperature and under dim light for 25 days, demonstrating the synergistic effect of $EDAI_2$ and $Pb(OAc)_2$ in stabilizing γ-$CsPbI_3$ PSCs.

Received 1st June 2023
Accepted 6th June 2023

DOI: 10.1039/d3ta03249c

rsc.li/materials-a

Introduction

In the past few decades, organic–inorganic hybrid perovskite solar cells (PSCs) have made great progress, as illustrated by the fact that their power conversion efficiencies (PCEs) have risen from the initial 3.5% to 26%.[1–5] However, state-of-the-art perovskite devices often employ organic cations such as formamidinium (FA) and methylammonium (MA), which exhibit poor chemical and thermal stability, hindering their commercial application. Replacing these volatile organic cations with inorganic ions such as Cs and Ru has the potential to improve the intrinsic stability of perovskite devices.[6,7]

For inorganic cesium lead halide perovskites, cesium lead iodide ($CsPbI_3$) PSCs have attracted particularly widespread attention due to their tolerance to high temperatures and an ideal bandgap of ~1.73 eV, which is very suitable for tandem photovoltaic applications.[8–12] Although the performance of $CsPbI_3$ PSCs has surged to over 20%,[13,14] most high-performance devices are fabricated *via* the dimethylammonium iodide (DMAI)-assisted method, which limits the options for large-scale preparation.[8,15–18] Furthermore, the potential presence of the organic component DMA in the final $CsPbI_3$ films remains under debate.[19–23] Therefore, it is imperative to develop a plethora of preparation processes to adapt to complex industrial manufacturing and obtain highly phase-pure $CsPbI_3$ thin films. Consequently, You and colleagues reported that high efficiency (PCE = 15.7%) α-$CsPbI_3$ PSCs can be fabricated by employing a solvent-controlled growth of perovskite precursors under a dry environment. Moreover, the devices did not show an efficiency drop under continuous light soaking for more than 500 hours.[24] Liu *et al.* reported that careful control over the elemental composition and annealing environment enabled the fabrication of γ-$CsPbI_3$ solar cells with a PCE of 16.3%.[25] Alternatively, additives have also proven to be very effective in modulating the perovskite crystallization dynamics, resulting in the formation of high-quality perovskite films. Ho-Baillie and co-workers adopted a cation exchange growth method for fabricating high-quality γ-$CsPbI_3$ by introducing a methylammonium iodide (MAI) additive into the perovskite precursor solution, achieving 14.1% device efficiency.[7] Alternatively, Li *et al.* developed a mediator-antisolvent strategy in which MAI and phenyl-C_{61}-butyric acid methyl ester ($PC_{61}BM$) were used as additives introduced into the chlorobenzene antisolvent used for device fabrication. The method allowed to obtain high-quality and stable black-phase $CsPbI_3$ perovskite films with solar cell efficiencies reaching up to 16.04%.[26] Very recently, Luo's group demonstrated that adding formamidine acetate (FAAc) into the precursor solution improves the phase purity and electronic quality of γ-$CsPbI_3$ films. As

[a]Chair for Emerging Electronic Technologies, Technische Universität Dresden, Nöthnitzer Straße 61, 01187 Dresden, Germany. E-mail: yana.vaynzof@tu-dresden.de
[b]Leibniz-Institute for Solid State and Materials Research Dresden, Helmholtzstraße 20, 01069 Dresden, Germany

† Electronic supplementary information (ESI) available. See DOI: https://doi.org/10.1039/d3ta03249c

a result, the authors achieved a very high efficiency of over 18%.[6] However, despite the impressive achievements outlined above, a key limitation for their future application lies in the fact that all these methods rely on annealing at high temperatures (~340 °C) in order to ensure rapid volatilization of the organic components, which may inevitably trigger the formation of voids and pinholes in the perovskite film. Importantly, the high-temperature processing required to form $CsPbI_3$ by these methods made it necessary to employ the n-i-p architecture of photovoltaic devices. This architecture, however, exhibits several disadvantages, such as a poor thermal stability of the hole transport layers (*e.g.*, Spiro-MeOTAD) and incompatibility with applications in tandem devices, which predominantly rely on a p-i-n configuration.[17,18] Moreover, as compared to standard architecture n-i-p devices, the p-i-n structured solar cells do not rely on the use of undesired dopants in the carrier transport layers, which has been shown to negatively impact the device's stability and hysteresis.[27,28] Finally, inverted p-i-n devices can be realized entirely *via* low-temperature processing, which is a key requirement for their commercialization on a large scale as well as their application on flexible substrates.[4,29–31] Therefore, it is imperative to develop low-temperature (<200 °C) processes to prepare $CsPbI_3$ PSCs based on a p-i-n architecture.

Huang's group reported a facile method to stabilize α-$CsPbI_3$ films at low temperatures (~100 °C) with a p-i-n structure *via* a small amount of sulfobetaine zwitterion used as an additive in perovskite solution. This method resulted in the solar cells with a PCE of 11.4%.[32] Alternatively, a thermal evaporation process has also been proven to be a suitable method for fabricating $CsPbI_3$ films at low temperatures. Unold *et al.* prepared stable γ-$CsPbI_3$ films at 50 °C by elaborately controlling the deposition ratios of the CsI and PbI_2 during the evaporation process. As a result, the authors obtained an efficiency exceeding 12%.[33] In recent years, we also reported on the vapor deposition of $CsPbI_3$ *via* a low-temperature process (~100 °C) and proposed a ternary source (CsI, PbI_2, and phenylethylammonium iodide) co-evaporation method to prepare stable γ-$CsPbI_3$ films, achieving a 15% device efficiency.[34] Nevertheless, the efficiency of devices fabricated at low temperatures still lags far behind those made at high temperatures.

Therefore, fabricating high-efficiency pure $CsPbI_3$ PSCs at a low temperature (<200 °C) remains challenging. Notably, utilizing alternative, non-halide lead sources opens an opportunity to address this issue. For example, lead acetate ($Pb(OAc)_2$) is intensively used to fabricate high-quality $MAPbI_3$ films *via* a rapid process that relies on a low annealing temperature – a consequence of an accelerated crystallization process facilitated by the removal of the volatile methylammonium acetate (MAOAc).[35–40] Similarly, $Pb(OAc)_2$ has also been utilized as a cost-effective lead source to replace the traditionally used PbI_2 for the fabrication of $FA_xMA_{1-x}PbI_3$ and $FA_{1-x}Cs_xPbI_3$ devices, resulting in high-quality perovskite films and good photovoltaic performance.[38,39,41] Other studies explored the use of $Pb(OAc)_2$ as an additive in perovskite precursor solutions in order to improve the morphology and stability of the films.[42–44] Despite these promising results, the use of $Pb(OAc)_2$ in fabricating inorganic perovskites remains rare, and the related film formation mechanisms are poorly understood.

In this work, we propose a low-temperature preparation method for high-quality and stable γ-$CsPbI_3$ films, using the long-chain organic cation ethane-1,2-diammonium iodide ($EDAI_2$) and replacing PbI_2 with a more cost-effective lead source $Pb(OAc)_2$ in the perovskite precursor solution. Our results indicate that the use of $EDAI_2$ and $Pb(OAc)_2$ results in the formation of $EDA(OAc)_2$, which escapes during the film formation process and promotes the formation of γ-$CsPbI_3$. At the same time, an excess $Pb(OAc)_2$ additive can further stabilize the γ-$CsPbI_3$ perovskite. Improved crystallinity, morphology and reduced charge carrier recombination are demonstrated for films with an optimal $Pb(OAc)_2$ excess. Importantly, by replacing PbI_2 with $Pb(OAc)_2$ as the Pb source, we eliminate the need to employ dimethylformamide (DMF) – a highly toxic solvent – and rely only on the significantly less toxic dimethyl sulfoxide (DMSO) for the processing of the $CsPbI_3$ films. By further optimizing the type of hole transport layer (HTL) used for inverted architecture device fabrication, we obtained an efficiency of 16.57%, which surpasses those previously reported for inverted γ-$CsPbI_3$ PSCs.[32–34,45–47] The optimized $CsPbI_3$ devices also showed improved stability, with encapsulated solar cells maintaining 97% of their initial efficiency at room temperature and under dim light illumination for 25 days of aging. These findings provide a new method to fabricate high-efficiency and stable inorganic perovskite solar cells using $Pb(OAc)_2$ and with low-temperature processes.

Results and discussion

Impact of $Pb(OAc)_2$ excess on film formation of $CsPbI_3$

To investigate the effect of $Pb(OAc)_2$ excess, we fabricated perovskite films using $EDAI_2$, CsI, and $Pb(OAc)_2$ with a stoichiometry ratio of 1 : 1 : *X* in a DMSO solution (Fig. 1a), in which *X* denotes the relative proportion of $Pb(OAc)_2$ to the other precursors that were introduced in equant amounts. Test experiments revealed that using a perfectly stoichiometric ratio of 1 : 1 : 1 did not lead to the formation of a perovskite, so a series of different *X* values with varying $Pb(OA_C)_2$ excess (*e.g.*, 1.1, 1.15, 1.2, 1.25, and 1.3) were studied. The perovskite films were fabricated in a one-step process and subsequently annealed at 60 °C for 5 min, and then at 180 °C for another 3 min in dry air, as shown schematically in Fig. 1b. Detailed processing procedures are provided in the Experimental section.

To examine the evolution of the film formation before and during the annealing process, X-ray diffraction (XRD) measurements for perovskite films undergoing different thermal annealing temperatures and times were carried out. As is shown in Fig. 2a, the as-deposited wet film (prior to annealing) contains DMSO-related intermediate products.[39,48–50] When preheating the film at 60 °C, the intermediate products vanish, while crystalline PbI_2 is formed. As the annealing temperature is increased to 180 °C, the PbI_2 is rapidly decreased and already after 30 s can no longer be observed. At the same time, signals associated with $CsPbI_3$ and $Pb(OAc)_2$ appear. The accompanying images and top-

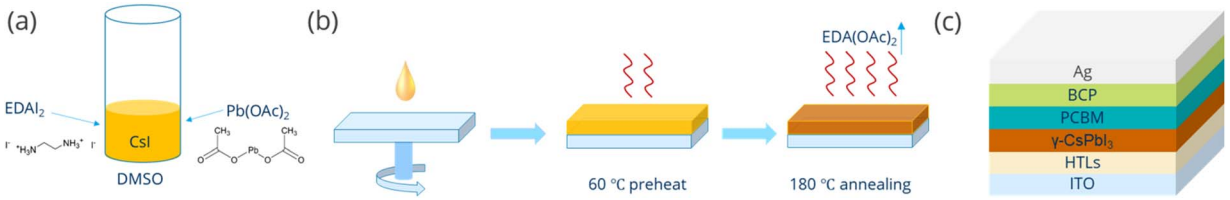

Fig. 1 Schematic illustration of the (a) precursor preparation and (b) film formation procedure. (c) Structure of the device in this work.

view SEM micrographs of the films under the same annealing conditions are shown in Fig. S1.† The images illustrate the evolution of the layer's morphology both in terms of the increase in grain size and the elimination of pinholes from the film's microstructure once the 3 min annealing at 180 °C is completed.

To further understand the process taking place during the preheating, we characterized the preheated film (60 °C and 5 min) using Fourier-transform infrared spectroscopy (FTIR). Fig. 2b shows several pronounced characteristic peaks associated with COO^- and N–H vibrations, which suggests that an $EDA(OAc)_2$ product may form in the preheated film. To further verify whether $EDA(OAc)_2$ can be removed from the film during the subsequent annealing process (*i.e.*, at 180 °C), we performed thermogravimetric analysis (TGA) for the $EDA(OAc)_2$ intermediate product. As shown in Fig. S2,† the initial decomposition temperature (defined by T at 95% weight) for $EDA(OAc)_2$ is 137.7 °C, which confirms that $EDA(OAc)_2$ is thermally unstable and can be easily removed from the perovskite film when the annealing temperature is higher (180 °C). These measurements suggest that the role of $EDA(OAc)_2$ in the formation of $CsPbI_3$ is similar to that of MAAc in the fabrication of $MAPbI_3$ perovskite based on the $Pb(OAc)_2$ recipe[35,36] – in both cases, these species can be removed from the perovskite film during the annealing process. Based on these results, we propose that the crystallization process occurs *via* the following route:

$$X\,Pb(OAc)_2 + EDAI_2 + CsI \rightarrow CsPbI_3 + EDA(OAc)_2\uparrow + (X-1)\,Pb(OAc)_2\ (X>1)$$

To characterize the crystalline structure of the $CsPbI_3$ films formed with different amounts of $Pb(OAc)_2$ excess, XRD measurements were carried out, with the results shown in Fig. 2c. We observe that for $X > 1.1$ the diffractograms exhibit characteristic perovskite peaks at ~14.3° and ~29.0°, corresponding to the (110) and (220) planes of orthorhombic γ-$CsPbI_3$, respectively. It can be seen that the intensity of the (110) and (220) peaks increases with a rise in the $Pb(OAc)_2$ excess, which suggests that the excessive $Pb(OAc)_2$ facilitates the preferred orientation along the (110) and (220) planes in the final perovskite film. For lower $Pb(OAc)_2$ amounts (*e.g.*, $X = 1.1$), no (110) and (220) diffraction peaks are observed, which implies that a significant excess of $Pb(OAc)_2$ is a prerequisite for the formation of γ-$CsPbI_3$ perovskite. Examining the diffractograms at low angles (below 12°, Fig. S3a†) reveals that a small fraction of the films is δ-phase $CsPbI_3$, with higher X ratios resulting in a small fraction of this unfavorable phase. Notably, the patterns show no characteristic 2D peaks in the final $CsPbI_3$ films, suggesting that $EDAI_2$ is not incorporated into the perovskite lattice. Moreover, for films with a large excess of $Pb(OAc)_2$ ($X \geq 1.25$), a diffraction peak at 7.5° can be observed, which corresponds to $Pb(OAc)_2$. To further confirm that no 2D phases are present in the final $CsPbI_3$ film, grazing incidence X-ray diffraction (GIXRD) measurements were carried out on the $X = 1.2$ sample by varying the incidence angle Ω from 0.2 to 2.0 (Fig. S3b†). The low-incidence angles are more surface sensitive, while the high angles probe more of the bulk. It can be seen that no characteristic 2D signals are detected from the surface to the bulk, which means that there are no 2D perovskite phases formed in the final film. We note that we observe a very small amount of δ-phase $CsPbI_3$ at the bulk of the film, yet, as will be shown later, this does not seem to impact either the optoelectronic quality or the stability of the perovskite.

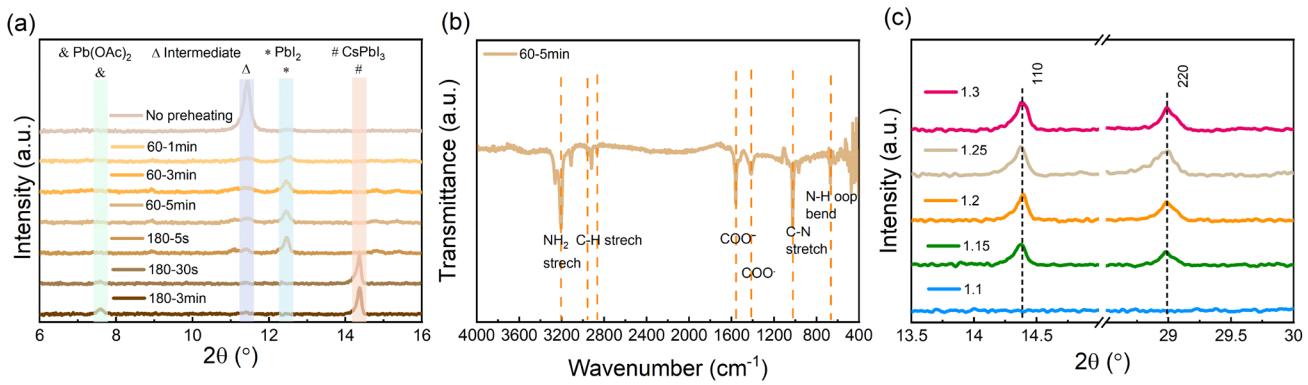

Fig. 2 (a) X-ray diffraction (XRD) patterns of perovskite films on ITO substrates with different heating temperatures and times, (b) Fourier-transform infrared spectroscopy of the intermediate perovskite film (after the perovskite precursors were deposited, the film was preheated at 60 °C for 5 min), and (c) XRD patterns of final $CsPbI_3$ on glass substrates with different amounts of $Pb(OAc)_2$ excess.

To confirm the absence of $EDAI_2$ in the perovskite layers, we performed X-ray photoemission spectroscopy (XPS) measurements on the preheated and annealed films with different $Pb(OAc)_2$ excess amounts (Fig. S4, ESI†). Regardless of the exact amount of $Pb(OAc)_2$ excess, the preheated films show obvious nitrogen signals (corresponding to atomic percentages ranging from 10 to 15%) before the annealing at 180 °C, indicating that the EDA cation is present in the films (Fig. S4†). After annealing at 180 °C for 3 minutes, no nitrogen could be detected in the films, confirming that EDA is no longer present. Considering that XPS is a surface-sensitive technique, we performed XPS depth profiling on the 1.2 sample in order to examine whether EDA might be present in the bulk of the film. We observe no nitrogen signals, neither at the surface (Fig. S5†) of the layer nor in the bulk (Table S1†), which confirms that no EDA cations remain in the final perovskite film. The O 1s spectrum collected at the surface of the film exhibits two peaks. While the high binding energy peak is likely associated with surface contamination, the low binding energy peak at ~530 eV may arise from either the $Pb(OAc)_2$ precursor or DMSO solvent. Considering that no sulfur signal is observed in the XPS spectra, the latter can be ruled out, suggesting that these oxygen species are associated with the $Pb(OAc)_2$ precursor. We note that the low binding energy peak is unlikely to be related to the formation of lead oxide since it requires much higher temperatures (~350 °C) than those used by us during layer fabrication.[44] The gradual increase in the oxygen and lead atomic concentrations with increasing $Pb(OAc)_2$ ratio confirms that excess $Pb(OAc)_2$ in the precursor solution also results in its excess in the final film, in agreement with the XRD results (Fig. S4†).

To further confirm that no EDA cation was left in the final perovskite film, proton nuclear magnetic resonance (H-NMR) measurements of both the $CsPbI_3$ film and the intermediate product $EDA(OAc)_2$ were carried out, with the results shown in Fig. S6.† The $EDA(OAc)_2$ product displays a very strong NMR peak associated with $-CH_2-$ ($\delta = 2.7$ ppm) and $-NH_3^+-$ ($\delta = 5.4$ ppm) originating from EDA^{2+} and a CH_3COO^- ($\delta = 1.80$ ppm) peak, which is consistent with previous reports in literature.[51] The H-NMR signals of $-CH_2-$ and $-NH_3^+-$ disappear entirely in the final $CsPbI_3$ perovskite film, which confirms that no EDA cation remains in the final perovskite layer. We note that there are two additional peaks in the final $CsPbI_3$ film. The peak at ~3.3 ppm corresponds to an impurity such as water in the DMSO-d6 solvent. The weak but non-negligible peak at 1.74 ppm corresponds to CH_3COO^-. This signal arises from the excess of $Pb(OAc)_2$ present in the film, which agrees with both the XRD and XPS measurements.

Concerning the crystallinity changes observed for samples with different amounts of $Pb(OAc)_2$ excess, the microstructure of the layers can be expected to play a role as well. To characterize it, we performed scanning electron microscopy (SEM) measurements, and the representative images are shown in Fig. 3. It can be seen that the perovskite films show many obvious pinholes when fabricated using smaller amounts of $Pb(OAc)_2$ excess. These pinholes gradually disappear as the content of $Pb(OAc)_2$ increases. For $X = 1.2$, no pinholes can be observed and the film consists of relatively large and uniform crystal domains. A further rise in the $Pb(OAc)_2$ excess has a negative impact on the microstructure. We observe the appearance of small additional domains at the surface, which appear different in contrast to the perovskite domains. To examine the composition of these small domains on the surface, energy-dispersive X-ray spectroscopy (EDX) spectra were recorded at different sample locations. As is shown in Fig. S7,† the small domains exhibit an additional oxygen-related signal which is not present in the large domains associated with the perovskite. These measurements suggest that $Pb(OAc)_2$ remains on the perovskite crystal surface, consistent with the XRD and H-NMR results. To examine the microstructure in the

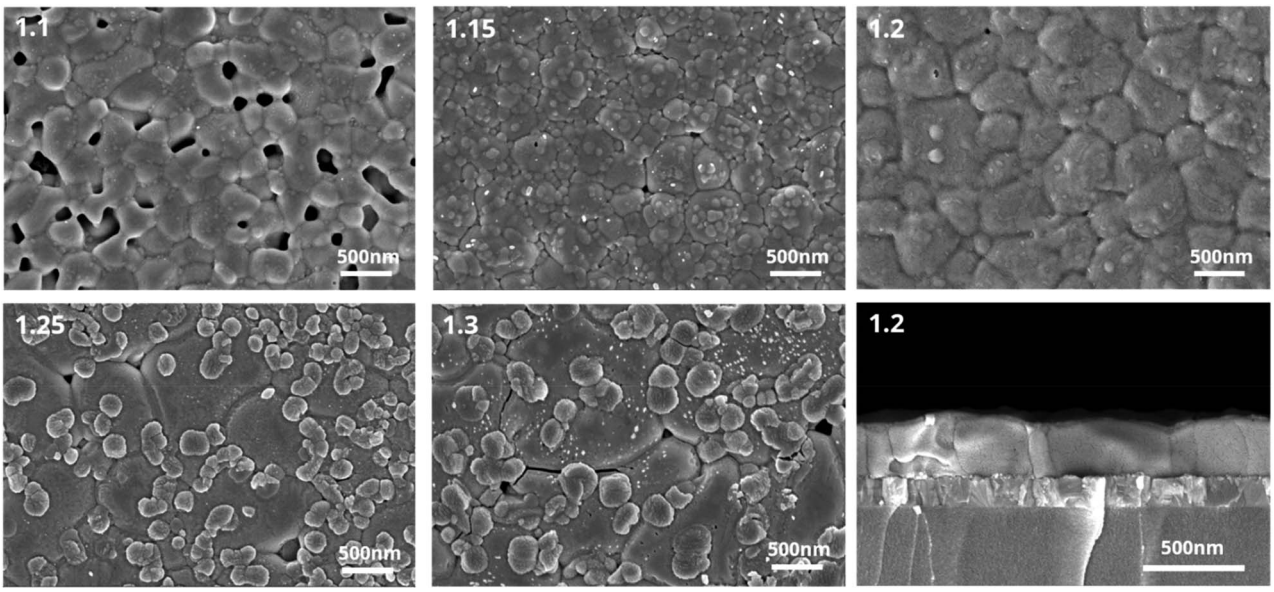

Fig. 3 Scanning electron microscopy images of different $Pb(OAc)_2$ ratios ($X = 1.1$, 1.15, 1.2, 1.25 and 1.3). Cross-sectional images of 1.2 samples on glass/ITO.

direction of charge transport, cross-sectional SEM was also performed on the $X = 1.2$ sample. Samples with this composition show very compact crystal packing, without voids at the interface to the substrate or in the bulk, with many domains protruding throughout the entire layer thickness. This suggests that the $X = 1.2$ stoichiometry enables the formation of high-quality perovskite films with relatively few boundaries in the direction of charge transport.

To investigate the optical properties of the perovskite films with different amounts of $Pb(OAc)_2$ excess, absorption, steady-state and time-resolved photoluminescence (TRPL) measurements were performed. As is shown in Fig. 4a, no significant changes in the UV-vis absorption spectra could be observed. The absorption edges are located at approximately 715 nm, corresponding to a 1.73 eV bandgap, consistent with other reports examining the optical properties of γ-$CsPbI_3$.[10,52,53] PL spectra show no shift in the peak position for samples with different $Pb(OAc)_2$ excess amounts, which agrees with the absence of bandgap variation in the absorption spectra. The PL intensity gradually increases with X rising with the maximum achieved at $X = 1.2$, suggesting that the presence of a certain fraction of excess $Pb(OAc)_2$ can passivate defects in the perovskite bulk or at the domain boundaries, thus reducing the degree of non-radiative recombination.[44,54] However, with further increase in the $Pb(OAc)_2$ excess, the PL intensity is reduced, which we associate with the poorer film microstructure and the presence of $Pb(OAc)_2$ domains.[44,55] Fig. 4c displays TRPL decay curves for different amounts of $Pb(OAc)_2$ excess. Considering that the curves show a non-monoexponential decay, the lifetime is evaluated using an average lifetime (τ_{ave}) and the corresponding fitting results are shown in Fig. S8 and Table S2.† Compared to other amounts of $Pb(OAc)_2$ excess, the 1.2 film shows longer τ_{ave}, consistent with a reduced density of trap states in the 1.2 perovskite film.[56,57] To evaluate the optical properties of the optimal $CsPbI_3$ film ($X = 1.2$) in more detail, the film was characterized using photothermal deflection spectroscopy (PDS), as shown in Fig. S9.† The Urbach energy (Eu) extracted from the PDS spectrum is ~18.28 meV – lower than previously reported values for inorganic lead halide perovskites.[58–61] A lower Urbach energy corresponds to a reduced energetic disorder, suggesting a reduced defect density in the $X = 1.2$ films.[35,62,63]

Photovoltaic performance of γ-$CsPbI_3$ devices with different amounts of $Pb(OAc)_2$ excess

To characterize the photovoltaic performance of the films fabricated using different amounts of $Pb(OAc)_2$ excess, they were integrated into solar cells with the inverted structure of glass/ITO/MeO-2PACz (MeO_2)/γ-$CsPbI_3$/$PC_{61}BM$/bathocuproine (BCP)/Ag. We note that we utilized a 1.0 M concentration and a CsI:$EDAI_2$ ratio of 1.0 in the perovskite precursor solution, which were identified as optimal in the preliminary experiments shown in Fig. S10 and S11 in the ESI.† The photovoltaic performance parameters of devices with different amounts of $Pb(OAc)_2$ excess are summarized in Fig. 5a–d. Devices with $X = 1.1$ show an average open-circuit voltage (V_{OC}) of 0.85 V, which suggests significant non-radiative losses, in agreement with the lowest PL intensity, shortest average carrier lifetime, and poor layer morphology. Gradually increasing the $Pb(OAc)_2$ ratio to 1.2, the V_{OC} is increased, reaching a maximum of 1.24 V. The short-circuit current density (J_{SC}) and fill factor (FF) are also dramatically increase, reaching J_{SC}s up to 18 mA cm^{-2} and FFs of 80%. With a further increase in the $Pb(OAc)_2$ excess ($X > 1.2$), the performance is reduced, with significant drops in V_{OC} and FF. This indicates that samples with too much $Pb(OAc)_2$ excess might exhibit higher recombination losses, resulting in a lower V_{OC} and FF and, consequently, an overall inferior efficiency.[44,64,65]

Optimization of hole transport layers for $CsPbI_3$ PSCs

Considering that the choice of substrates may strongly impact on the perovskite film formation,[66–68] we chose the $X = 1.2$ stoichiometry samples to investigate four different hole transport layers (HTLs): inorganic (NiO_x), polymer (PTAA), self-assemble monolayers (SAMs, MeO-2PACz, in the following termed 'MeO_2'), and inorganic/SAMs hybrids (NiO_x/MeO_2 – where the NiO_x layer is first deposited on ITO and then coated with a MeO_2 SAM). As is detailed in the Experimental section, these HTLs were spin-coated on pre-cleaned ITO substrates prior to the deposition of the perovskite layer. To evaluate the impact of the HTL on the perovskite films' microstructure, the layers were characterized by SEM. As is shown in Fig. 6, perovskite layers deposited on NiO_x exhibited a multitude of pinholes

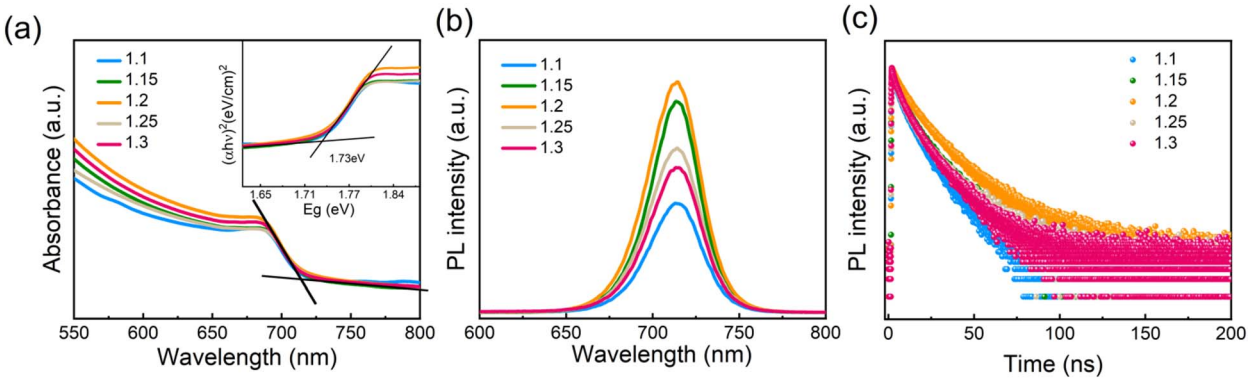

Fig. 4 (a) UV-vis absorbance spectra (inset: Tauc plot for $CsPbI_3$ films with different amounts of $Pb(OAc)_2$ excess) and (b) steady state and (c) time-resolved photoluminescence emission (PL) spectra of different $Pb(OAc)_2$ ratio (1.1, 1.15, 1.2, 1.25 and 1.3) samples.

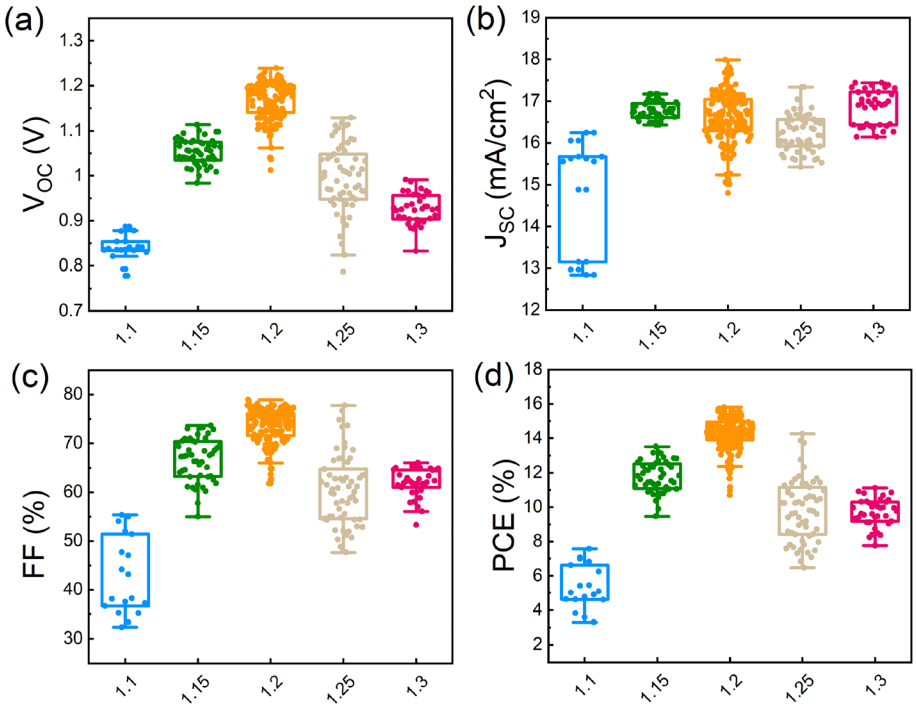

Fig. 5 Photovoltaic performance parameters: (a) V_{OC}, (b) J_{SC}, (c) FF and (d) PCE distributions of different $Pb(OAc)_2$ ratios (1.1, 1.15, 1.2, 1.25 and 1.3). A total of 350 devices were measured.

that could be observed on the surface of the perovskite film, as well as voids that could be seen in the cross-sections. The organic HTLs (PTAA and MeO_2) result in better-quality films with no visible pinholes and voids. However, both films exhibit small domains at the film's surface and/or bulk. EDX measurements reveal that these domains are associated with $Pb(OAc)_2$ due to a clear presence of O in these spectra (Fig. S12–S14†). Finally, the deposition of $CsPbI_3$ on the NiO_x/MeO_2 hybrid substrates results in a uniform and compact microstructure with no visible pinholes or small $Pb(OAc)_2$ domains at the surface or bulk. To further understand how the choice of the HTL influences the morphology of the perovskite layer, we performed contact angle measurements for the different HTLs, with the results shown in Fig. S15.† Compared to other HTLs, the PTAA substrate displays the largest contact angle, leading to enlarged perovskite grain size, which is consistent with previous reports that hydrophobic surfaces with increased surface tension can lead to an increased average size of the perovskite domains.[66,69–72] NiO_x, MeO_2, and NiO_x/MeO_2 HTLs show almost identical contact angles, thus resulting in a negligible change in the average perovskite grain size. However, there are many pinholes and voids in the perovskite film deposited on NiO_x, which is likely related to the presence of surface defects in the NiO_x layer.[73,74] To investigate the impact of the HTL on the crystalline structure of the perovskite layer, we performed XRD measurements (Fig. S16†). The resultant diffractograms are very

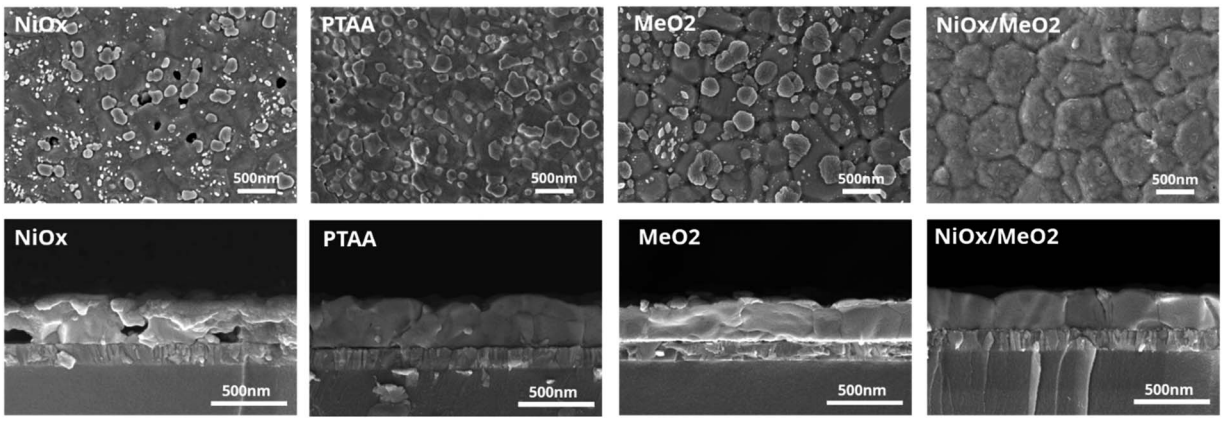

Fig. 6 Top view and cross-section SEM images of $CsPbI_3$ films deposited on different hole transport layers (NiO_x, PTAA, MeO_2, and NiO_x/MeO_2).

similar, with diffraction peaks associated with $Pb(OAc)_2$ and γ-$CsPbI_3$ and no additional features such as δ-$CsPbI_3$, indicating that the different HTLs do not influence the crystal structure of perovskite even though the perovskite morphology is changed, which is consistent with previous reports.[69]

To compare the performance of the solar cells with the four different types of HTLs, we fabricated devices with $X = 1.2$ for each of the HTLs. As shown in Fig. 7a–d, devices manufactured on NiO_x show the worst performance, particularly evident in their lower V_{OC}s and FFs. This is a direct consequence of the poor film coverage and the many voids at the interface to the HTL. Devices that utilize the PTAA, MeO_2, and NiO_x/MeO_2 HTLs exhibit much better photovoltaic performance. In particular, in the case of the hybrid NiO_x/MeO_2 HTLs, the devices display much higher J_{SC}s and FFs, thus resulting in an overall higher performance. The best performing device was obtained with NiO_x/MeO_2 hybrid HTLs (Table 1), achieving an efficiency of 16.57% with a V_{OC} of 1.18 V, a J_{SC} of 17.56 mA cm^{-2}, and a FF of 79.74%. To our knowledge, this is among the highest performances reported for γ-$CsPbI_3$ PSCs with an inverted architecture.[33,34] Importantly, the $CsPbI_3$ PSCs deposited on the different HTLs show negligible hysteresis (Fig. 7e). Fig. 7f displays the external quantum efficiency (EQE) spectrum and integrated J_{SC} curve for the champion $CsPbI_3$ solar cell deposited on NiO_x/MeO_2. The integrated J_{SC} is calculated to be 17 mA cm^{-2}, which is in excellent agreement with the value extracted from the *J–V* curve. Fig. 7g shows the device's maximum power point (MPP) tracking, resulting in a stabilized power output of 15.60%, which is higher than previously reported values for inverted architecture γ-$CsPbI_3$ PSCs.[29] A continuous MPP tracking for a period of 12 hours is shown in Fig. S17.†

Table 1 Photovoltaic performance parameters of champion cells on different HTLs (NiO_x, PTAA, MeO_2 and NiO_x/MeO_2)

Different HTLs	V_{OC} [V]	J_{SC} [mA cm^{-2}]	FF [%]	PCE [%]
NiO_x-forward	1.03	16.78	62.25	10.74
NiO_x-reverse	1.05	16.78	63.06	11.13
PTAA-forward	1.17	16.85	77.26	15.18
PTAA-reverse	1.17	16.85	78.10	15.46
MeO_2-forward	1.18	17.15	71.50	14.50
MeO_2-reverse	1.20	17.15	76.60	15.81
NiO_x/MeO_2-forward	1.15	17.56	75.25	15.22
NiO_x/MeO_2-reverse	1.18	17.56	79.74	16.57

To understand the origin of the enhanced performance of the devices with NiO_x/MeO_2, we examined their properties in more detail. First, we characterized the morphology of the four different HTLs by atomic force microscopy (AFM). As shown in Fig. S18,† the microstructures of NiO_x and NiO_x/MeO_2 are very similar, with essentially the same root mean square (RMS) roughness. The PTAA and MeO_2 layers are slightly smoother, but their performance is inferior to that of NiO_x/MeO_2, suggesting that performance differences are not related to the layer morphology. Next, we examined the energetic alignment at the HTL/perovskite interface and performed ultraviolet photoemission spectroscopy (UPS) measurements on the different HTLs and the perovskite layer, with the results displayed in Fig. S19 and Table S4.† It can be seen that among the four extraction layers, only PTAA shows a slight energetic shift as compared to the perovskite layer. In contrast, the other layers show excellent energetic alignment. Despite this energetic offset, PTAA-based devices deliver high V_{OC} averaging 1.17 V,

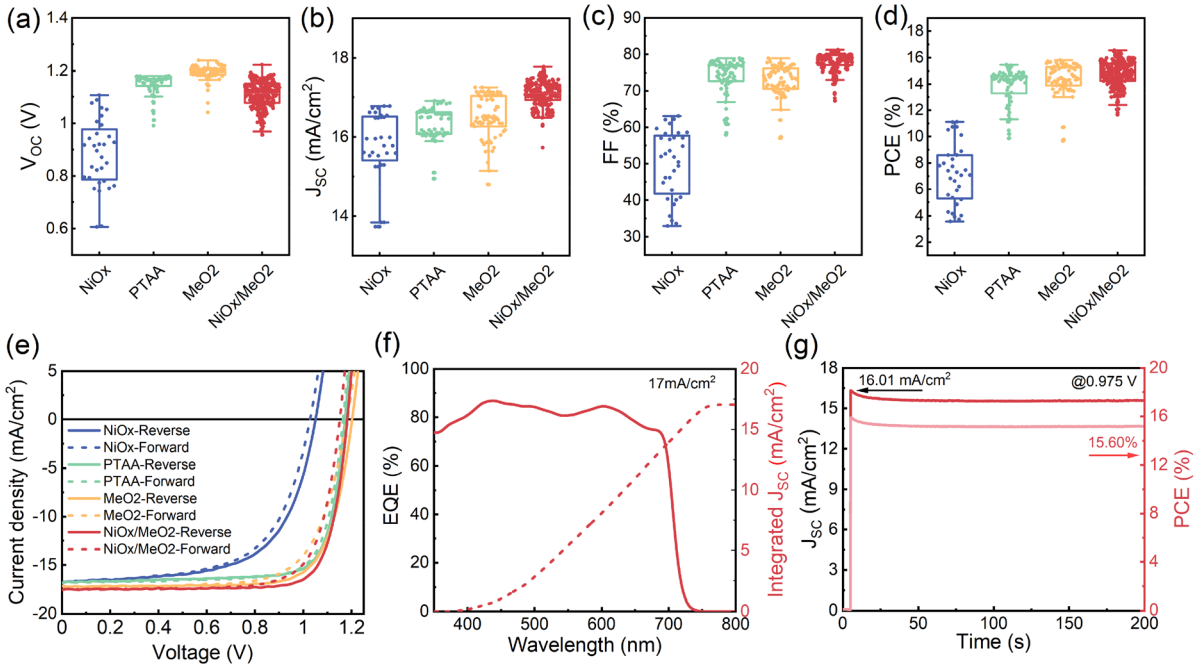

Fig. 7 Photovoltaic performance parameter: (a) V_{OC}, (b) J_{SC}, (c) FF, and (d) PCE distribution of $X = 1.2$ $CsPbI_3$ PSCs deposited on different HTLs (NiO_x, PTAA, MeO_2, and NiO_x/MeO_2). A total of 450 devices were measured. (e) *J–V* characteristic curves of champion cells on different HTLs (NiO_x, PTAA, MeO_2, and NiO_x/MeO_2). (f) EQE spectrum and (g) MPP tracking of the 1.2 champion device.

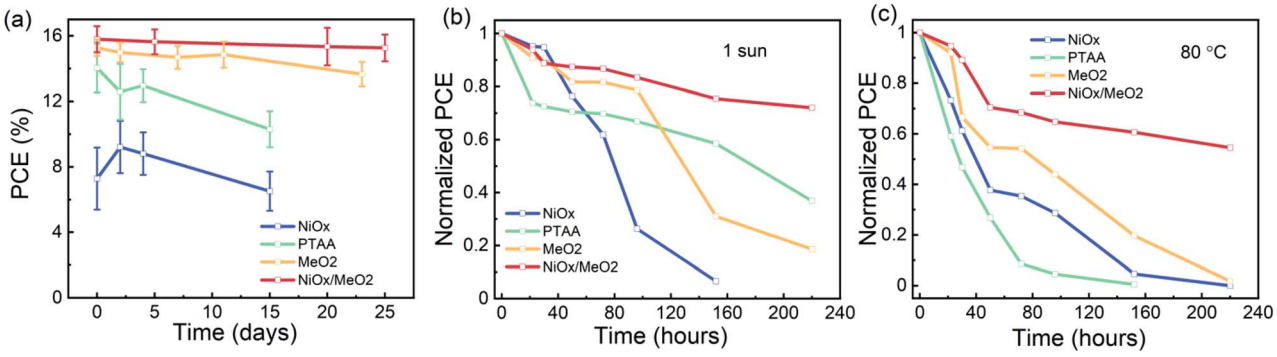

Fig. 8 Evolution of the PCE of encapsulated devices on different HTLs kept at (a) room temperature, under dim light, (b) under 1 sun illumination and (c) on an 80 °C hotplate.

due to the ability of the perovskite layer to compensate for interfacial energetic offsets by forming an electronic dipole.[75] Despite the energetic alignment of NiO_x and NiO_x/MeO_2 being very similar, the former exhibits a far lower V_{OC}, suggesting this loss is related to non-radiative recombination at the interface due to the increased density of defects. Indeed, previous literature reports suggest that NiO_x exhibits a large density of oxygen vacancies and other traps in the NiO_x layer.[76–78]

To investigate the trap densities in the perovskite films deposited on the four different HTLs, hole-only devices with the architecture of ITO/HTLs/perovskite/Spiro-OMeTAD/Au were fabricated, with the corresponding *J–V* curves shown in Fig. S20.† The trap densities (N_t) can be obtained according to the following equation: $V_{TFL} = eN_tL^2/2\varepsilon\varepsilon_0$, where V_{TFL} is the trap-filling voltage, e is the elementary charge, L is the thickness of the perovskite layer, ε_0 is the relative dielectric constant, and ε is the vacuum permittivity.[23] The hole trap densities of the $X = 1.2$ $CsPbI_3$ samples on NiO_x, PTAA, MeO_2, and NiO_x/MeO_2 are 1.47 $\times$ 10^{15} cm^{-3}, 1.16 $\times$ 10^{15} cm^{-3}, 1.01 $\times$ 10^{15} cm^{-3} and 4.66 $\times$ 10^{14} cm^{-3}, respectively. Among the different HTLs, devices based on the NiO_x/MeO_2 HTL show a lower trap density in the final perovskite layer, contributing to the higher photovoltaic performance of the NiO_x/MeO_2 solar cells.

While the new method for fabricating γ-$CsPbI_3$ by a synergetic stabilization *via* the use of $Pb(OAc)_2$ excess and $EDAI_2$ shows the potential for future tandem photovoltaic applications, it is important to consider the long-term stability of the devices. To gain initial insights into the stability of the devices, we monitored the performance of encapsulated devices that were kept at room temperature under dim illumination (conditions are shown in Fig. S21†) for a period of 25 days. As shown in Fig. 8a, devices based on a NiO_x/MeO_2 HTL exhibited the highest stability, maintaining ~97% of their initial PCE for this period of time. Furthermore, we also investigated the light and thermal stability of $X = 1.2$ photovoltaic devices fabricated using the four different HTLs. When exposed to continuous illumination at one sun for 220 hours, the $X = 1.2$ devices maintained ~70% of their initial performance, while devices based on NiO_x degraded completely (Fig. 8b). After continuous heating at 80 °C for 220 hours, the $X = 1.2$ $CsPbI_3$ devices with a NiO_x/MeO_2 HTL maintain approximately 55% of their initial efficiency, while the devices based on all other HTLs are completely degraded (Fig. 8c).

To investigate the origin of the different light and thermal stability of the devices based on the various HTLs, SEM and XRD measurements were performed on perovskite films deposited on the different HTLs under continuous one sun illumination and 80 °C heating at various degradation times. As can be seen in Fig. S22–S24,† as compared to the other HTLs, perovskite films deposited on NiO_x/MeO_2 show better film coverage (*i.e.*, no pinholes) and a better retention of the perovskite microstructure after exposure to light and heat. The improved microstructure has been linked to enhanced stability both against environmental factors such as moisture and oxygen as well as illumination.[79–83]

Conclusions

To summarize, we reported on a new method to fabricate inorganic $CsPbI_3$ perovskites *via* a low-temperature process that synergistically utilizes $Pb(OAc)_2$ and $EDAI_2$. By adjusting the amount of $Pb(OAc)_2$ excess and selecting the optimal HTL, the microstructure of the perovskite layers could be improved, resulting in high-quality perovskite films with excellent optoelectronic properties. The $EDAI_2 : CsI : Pb(OAc)_2 = 1 : 1 : 1.2$ perovskite solar cells reached a high photovoltaic performance of up to 16.57%, which is among the highest previously reported efficiencies for γ-$CsPbI_3$ inverted PSCs. Moreover, the devices also exhibited enhanced stability and minimal hysteresis. These findings provide a new strategy to stabilize $CsPbI_3$ using a low-temperature process, paving the way for their future application both in tandem configurations and on flexible substrates.

Experimental section

Materials

ITO substrates were obtained from PsiOTech Ltd. $PC_{61}BM$ (>99.5%) was bought from Luminescence Technology Crop. PTAA, NiO_x and MeO-2PACz (MeO_2) were purchased from Sigma-Aldrich, Liaoning Youxuan Crop. and TCI, respectively. Lead(II) actate (>98%) was obtained from TCI company. Cesium iodide (99.999%, metals basis) was bought from Alfa Aesar.

Ethane-1,2-diammonium iodide was purchased from Greatcell Solar Materials. Chlorobenzene, toluene, dimethyl sulfoxide, and isopropanol were bought from Acros Organics. All materials were used without further purification.

Precursor preparation

For the PTAA hole transport layer, 1.5 mg PTAA powder was dissolved in 1 mL toluene solvent and then left on a hotplate at 70 °C overnight. For NiO_x precursors, 10 mg NiO_x powder was dispersed in 1 mL DI water and ultrasonicated at 40 °C for 10 min, followed by filtered with a 0.25 μm hydrophilic filter. For MeO_2 precursors, 1.5 mg MeO_2 powder was dissolved in 1 mL isopropanol, followed by ultrasonication at 40 °C for 10 min. For perovskite precursors, 259.81 mg (1 mmol) CsI, 315.92 mg (1 mmol) $EDAI_2$ and different ratios of $Pb(OAc)_2$ (357.82 mg, 1.1 mmol; 374.08 mg, 1.15 mmol; 390.35 mg, 1.2 mmol; 406.61 mg, 1.25 mmol; 422.88 mg, 1.3 mmol) were dissolved in 1 mL pure DMSO and then placed on a hotplate at 70 °C overnight. 20 mg PCBM powder was dissolved in 1 mL chlorobenzene solvent and stirred on a hotplate at 70 °C overnight. 0.5 mg BCP powder was dissolved in 1 mL isopropanol and put on a hotplate at 70 °C overnight.

Device fabrication

Patterned ITO was rinsed with acetone to remove the protective glue. Then it was ultrasonically cleaned with 2% Hellmanex detergent, deionized water, acetone, and isopropanol, followed by drying with a nitrogen gun. For the PTAA hole transport layer, the ITO substrates were treated with oxygen plasma for 10 min and then spin-coated with PTAA at 4000 rpm 30 s, followed by annealing at 100 °C for 10 min in a nitrogen filled glovebox. For nickel oxide, the clean ITO substrates were exposed to UV-ozone for 15 min and then coated with NiO_x aqueous at 5000 rpm for 40 s and annealed in ambient air at 120 °C for 10 min. For MeO_2, MeO_2 solution was coated on the plasma treated ITO substrates at 3000 rpm for 30 s and then annealed at 100 °C for 10 min in a nitrogen-filled glovebox. For NiO_x/MeO_2 hybrid HTLs, the MeO_2 was deposited on the NiO_x substrates at 3000 rpm for 30 s and then annealed in a glovebox at 100 °C for 10 min. Subsequently, the HTL coated substrates were transferred to a home-made drybox. For the PTAA coated layer, in order to increase wettability, 50 μL DMF was spin-coated on substrates at 4000 rpm for 30 s before perovskite deposition. For the perovskite active layer, 25 μL precursors were spin-coated on the HTL deposited ITO substrates at 6000 rpm for 60 s, followed by annealing at 60 °C for 5 min and then at 180 °C for 3 min. Subsequently, the as-prepared perovskite films were transferred to a nitrogen filled glovebox for other layer deposition. 35 μL $EDAI_2$ solution (5 mg mL^{-1} in ethanol) was spin-coated on the perovskite layer at 4000 rpm for 30 s, followed by annealing at 100 °C for 5 min. Next, 25 μL $PC_{61}BM$ solution was dynamically spin-coated at 2000 rpm for 30 s, followed by annealing at 100 °C for 3 min. Finally, a 35 μL hole-blocking layer was dynamically deposited on substrates at 4000 rpm for 30 s, followed by an 80 nm thermally evaporated Ag cathode (Mantis evaporator, base pressure of 10^{-7} mbar). The as-prepared photovoltaic devices were sealed in a glovebox using a transparent clean encapsulation glass, encapsulated by a UV-hardened epoxy glue.

Photovoltaic device characterization

The EQE spectra of the devices were recorded using the monochromatic light of a halogen lamp from 400 nm to 800 nm, and the reference spectra were calibrated using a NIST-traceable Si diode (Thorlabs). *J–V* characteristics were recorded by using a computer controlled Keithley 2450 source measure unit under a solar simulator (Abet Sun 3000 Class AAA solar simulator). The incident light intensity was calibrated *via* a Si reference cell (NIST traceable, VLSI) and tuned by measuring the spectral mismatch factor between a real solar spectrum and the spectral response of the reference cell and perovskite devices. All devices were scanned from short circuit to forward bias (1.3 V) and reverse with a rate of 0.025 V s^{-1}. No treatment was applied prior to measurements. The active area for all devices was 4.5 mm^2.

Scanning-electron microscopy (SEM) and energy-dispersive X-ray spectroscopy (EDX)

A SEM (Gemini 500, (ZEISS, Oberkochen, Germany)) with an acceleration voltage of 3 kV was utilized to obtain the surface and cross-sectional morphology images. For EDX measurements, an Oxford XMaxN-150 mm^2 detector with a solid angle of roughly 0.05 sr was used. The working distance was 8.5 mm and the acceleration voltage was 8 kV.

X-ray diffraction (XRD)

XRD patterns were recorded in ambient air by using a Bruker Advance D8 diffractometer equipped with a 1.6 kW Cu-anode (λ = 1.54060 Å) and a LYNXEYE_XE_T 1D-mode detector. The scans (2theta-omega mode, $2\theta = 5°–30°$, step size 0.01°, and 0.1 s per step) were measured in standard Bragg–Brentano geometry (goniometer radius 420 mm). For grazing incidence XRD, the parameters of scans are 2theta mode, $2\theta = 5°–12°$, step size 0.01°, and 0.1 s per step. The incidence angle (Ω) was fixed at 0.2°, 0.5°, 1° and 2°, respectively.

UV-vis absorption and photoluminescence measurements

A Shimadzu UV-3100 spectrometer was utilized to record the ultraviolet-visible (UV-vis) absorbance spectra. PL measurements were performed using a CW blue laser (405 nm, 20 mW, Coherent) as the excitation source. The PL signal was collected using a NIR spectrometer (OceanOptics). All samples were encapsulated to prevent the decomposition and enable all measurements to be carried out in ambient air at room temperature.

Time-correlated single photon counting (TCSPC)

A TCSPC setup is composed of a 375 nm laser diode head (Pico Quant LDHDC375), a PMA Hybrid detector (PMA Hybrid 40), a TimeHarp platine (all PicoQuant), and a Monochromator SpectraPro HRS-300 (Princeton Instruments). Perovskite films

on quartz were excited with the 375 nm laser diode and then the emission was collected by using the PMA hybrid detector. The pulse width is ≈44 ps, the power is ≈3 mW, and the spot size is ≈1 mm^2, so the excitation fluence is ≈0.132 J m^{-2}. The lifetimes were evaluated using reconvolution algorithms of FluoFit (PicoQuant).

Photothermal deflection spectroscopy (PDS)

The quartz substrates with perovskite films were mounted in a signal enhancing liquid (Fluorinert FC-770) filled quartz cuvette inside a N_2 filled glovebox. Then, the samples were excited using a tunable, chopped, monochromatic light source (150 W Xenon short arc lamp with a Cornerstone monochromator) and probed using a laser beam (635 nm diode laser, Thorlabs) propagating parallel to the surface of the sample. The heat generated through the absorption of light changes the refractive index of the Fluorinert liquid, resulting in the deflection of the laser beam. This deflection was measured using a position sensitive-detector (Thorlabs, PDP90A) and a lock-in amplifier (Amatec SR7230) and is directly correlated to the absorption of the film.

X-ray photoemission spectroscopy (XPS) measurement

The samples were transferred to an ultrahigh vacuum chamber (ESCALAB 250Xi from Thermo Scientific, base pressure: 2×10^{-10} mbar) for XPS measurements. XPS measurements were carried out using an XR6 monochromated Al Kα source ($h\nu = 1486.6$ eV) and a pass energy of 20 eV. Depth profiling and $X = 1.2$ sample surface etching were performed using an argon gas cluster ion beam with large argon clusters (Ar2000) and an energy of 4 keV generated by a MAGCIS dual mode ion source. These conditions were found to be optimal for the etching of both organic and perovskite layers.[57,84–86] During XPS depth profiling, the etching spot size was (2.5×2.5) mm^2 and the XPS measurement spot size was 650 μm. The measurement time per etch level was 8 min.

Author contributions

Z. Z. fabricated the perovskite films and devices and performed the SEM, XRD, UV-vis, PL, and PV measurements. R. J. and Q. A. assisted with device fabrication and characterization. Y. H. and M. D. performed the XPS and UPS measurements and data analysis. Y. L. performed the PDS measurement and J. B. evaluated the data. Z. Z. coordinated the project and created the first paper draft. Y. V. supervised the work and revised the manuscript. All authors contributed to the preparation of the manuscript.

Conflicts of interest

There are no conflicts to declare.

Acknowledgements

Z. Z. and R. J. are grateful for the financial support by the China Scholarship Council (scholarship #201806750012 and #201806070145, respectively). Z. Z. acknowledges a short-term scholarship from the Graduate Academy of Technische Universität Dresden and the Dresden Center for Nanoanalysis (DCN) for providing access to the SEM measurement. Z. Z. also thanks Dr Tian Luo, Dr Denys Usov, Dr Fabian Paulus, Dr Rongjuan Huang, Dr Katherina Haase, Dr Juanzi Shi, Raquel Dantas Campos and Shaoling Bai for very useful and fruitful discussions. This project has received funding from the European Research Council (ERC) under the European Union's Horizon 2020 Research and Innovation Programme (ERC grant agreement no. 714067, ENERGYMAPS) and the Deutsche Forschungsgemeinschaft (DFG) in the framework of the Special Priority Program (SPP 2196) project PERFECT PVs (#424216076).

Notes and references

1 National Renewable Energy Laboratory, https://www.nrel.gov/pv/cell-efficiency.html.
2 A. Kojima, K. Teshima, Y. Shirai and T. Miyasaka, *J. Am. Chem. Soc.*, 2009, **131**, 6050–6051.
3 S. Sidhik, Y. Wang, M. De Siena, R. Asadpour, A. J. Torma, T. Terlier, K. Ho, W. Li, A. B. Puthirath, X. Shuai, A. Agrawal, B. Traore, M. Jones, R. Giridharagopal, P. M. Ajayan, J. Strzalka, D. S. Ginger, C. Katan, M. A. Alam, J. Even, M. G. Kanatzidis and A. D. Mohite, *Science*, 2022, **377**, 1425–1430.
4 Q. Jiang, J. Tong, Y. Xian, R. A. Kerner, S. P. Dunfield, C. Xiao, R. A. Scheidt, D. Kuciauskas, X. Wang, M. P. Hautzinger, R. Tirawat, M. C. Beard, D. P. Fenning, J. J. Berry, B. W. Larson, Y. Yan and K. Zhu, *Nature*, 2022, **611**, 278–283.
5 Y. Zhao, F. Ma, Z. Qu, S. Yu, T. Shen, H. X. Deng, X. Chu, X. Peng, Y. Yuan, X. Zhang and J. You, *Science*, 2022, **377**, 531–534.
6 L. Duan, H. Zhang, M. Liu, M. Grätzel and J. Luo, *ACS Energy Lett.*, 2022, **7**, 2911–2918.
7 C. F. J. Lau, Z. Wang, N. Sakai, J. Zheng, C. H. Liao, M. Green, S. Huang, H. J. Snaith and A. Ho-Baillie, *Adv. Energy Mater.*, 2019, **9**, 1901685.
8 Y. Wang, Y. Chen, T. Zhang, X. Wang, Y. Zhao, Y. Wang, Y. Chen, T. Zhang, X. Wang and Y. Zhao, *Adv. Mater.*, 2020, **32**, 2001025.
9 Q. Zeng, X. Zhang, C. Liu, T. Feng, Z. Chen, W. Zhang, W. Zheng, H. Zhang and B. Yang, *Sol. RRL*, 2019, **3**, 1800239.
10 J. Zhang, G. Hodes, Z. Jin and S. Liu, *Angew. Chem., Int. Ed.*, 2019, **58**, 15596–15618.
11 C. Liu, Y. Yang, O. A. Syzgantseva, Y. Ding, M. A. Syzgantseva, X. Zhang, A. M. Asiri, S. Dai and M. Khaja Nazeeruddin, *Adv. Mater.*, 2020, **32**, 2002632.
12 W. Ahmad, J. Khan, G. Niu and J. Tang, *Sol. RRL*, 2017, **1**, 1700048.
13 Y. Cui, J. Shi, F. Meng, B. Yu, S. Tan, S. He, C. Tan, Y. Li, H. Wu, Y. Luo, D. Li and Q. Meng, *Adv. Mater.*, 2022, 2205028.
14 S. M. Yoon, H. Min, J. B. Kim, G. Kim, K. S. Lee and S. Il Seok, *Joule*, 2021, **5**, 183–196.
15 Y. Wang, M. Ibrahim Dar, L. K. Ono, T. Zhang, M. Kan, Y. Li, L. Zhang, X. Wang, Y. Yang, X. Gao, Y. Qi, M. Grätzel and Y. Zhao, *Science*, 2019, **365**, 591–595.

16 Y. Wang, X. Liu, T. Zhang, X. Wang, M. Kan, J. Shi and Y. Zhao, *Angew. Chem., Int. Ed.*, 2019, **58**, 16691–16696.
17 S. Fu, N. Sun, J. Le, W. Zhang, R. Miao, W. Zhang, Y. Kuang, W. Song and J. Fang, *ACS Appl. Mater. Interfaces*, 2022, **14**, 30937–30945.
18 S. Fu, J. Le, X. Guo, N. Sun, W. Zhang, W. Song and J. Fang, *Adv. Mater.*, 2022, **34**, 2205066.
19 X. Sun, Z. Shao, Z. Li, D. Liu, C. Gao, C. Chen, B. Zhang, L. Hao, Q. Zhao, Y. Li, X. Wang, Y. Lu, X. Wang, G. Cui and S. Pang, *Joule*, 2022, **6**, 850–860.
20 W. Ke, I. Spanopoulos, C. C. Stoumpos and M. G. Kanatzidis, *Nat. Commun.*, 2018, **9**, 1–9.
21 H. Bian, H. Wang, Z. Li, F. Zhou, Y. Xu, H. Zhang, Q. Wang, L. Ding, S. Liu, Z. Jin, H. Zhang, L. Ding, H. Bian, H. Wang, S. Liu, Z. Li, F. Zhou, Y. Xu, Q. Wang and Z. Jin, *Adv. Sci.*, 2020, **7**, 1902868.
22 A. R. Marshall, H. C. Sansom, M. M. McCarthy, J. H. Warby, O. J. Ashton, B. Wenger and H. J. Snaith, *Sol. RRL*, 2021, **5**, 2000599.
23 Y. Pei, Y. Liu, F. Li, S. Bai, X. Jian and M. Liu, *iScience*, 2019, **15**, 165–172.
24 P. Wang, X. Zhang, Y. Zhou, Q. Jiang, Q. Ye, Z. Chu, X. Li, X. Yang, Z. Yin and J. You, *Nat. Commun.*, 2018, **9**, 2225.
25 Q. Huang, F. Li, M. Wang, Y. Xiang, L. Ding and M. Liu, *Sci. Bull.*, 2020, **66**, 757–760.
26 T. Zhang, F. Wang, H. Chen, L. Ji, Y. Wang, C. Li, M. B. Raschke and S. Li, *ACS Energy Lett.*, 2020, **5**, 1619–1627.
27 N. Tessler and Y. Vaynzof, *ACS Appl. Energy Mater.*, 2018, **1**, 676–683.
28 M. Hatamvand, P. Vivo, M. Liu, M. Tayyab, D. Dastan, X. Cai, M. Chen, Y. Zhan, Y. Chen and W. Huang, *Vacuum*, 2023, 112076.
29 Y. Deng, S. Xu, S. Chen, X. Xiao, J. Zhao and J. Huang, *Nat. Energy*, 2021, **6**, 633–641.
30 S. Chen, X. Dai, S. Xu, H. Jiao, L. Zhao and J. Huang, *Science*, 2021, **373**, 902–907.
31 N.-G. Park and K. Zhu, *Nat. Rev. Mater.*, 2020, **5**, 333–350.
32 Q. Wang, X. Zheng, Y. Deng, J. Zhao, Z. Chen and J. Huang, *Joule*, 2017, **1**, 371–382.
33 P. Becker, J. A. Márquez, J. Just, A. Al-Ashouri, C. Hages, H. Hempel, M. Jošt, S. Albrecht, R. Frahm and T. Unold, *Adv. Energy Mater.*, 2019, **9**, 1900555.
34 Z. Zhang, R. Ji, M. Kroll, Y. J. Hofstetter, X. Jia, D. Becker-Koch, F. Paulus, M. Löffler, F. Nehm, K. Leo and Y. Vaynzof, *Adv. Energy Mater.*, 2021, **11**, 2100299.
35 P. Fassl, V. Lami, A. Bausch, Z. Wang, M. T. Klug, H. J. Snaith and Y. Vaynzof, *Energy Environ. Sci.*, 2018, **11**, 3380–3391.
36 W. Zhang, M. Saliba, D. T. Moore, S. K. Pathak, M. T. Hörantner, T. Stergiopoulos, S. D. Stranks, G. E. Eperon, J. A. Alexander-Webber, A. Abate, A. Sadhanala, S. Yao, Y. Chen, R. H. Friend, L. A. Estroff, U. Wiesner and H. J. Snaith, *Nat. Commun.*, 2015, **6**, 6142.
37 L. Zhao, D. Luo, J. Wu, Q. Hu, W. Zhang, K. Chen, T. Liu, Y. Liu, Y. Zhang, F. Liu, T. P. Russell, H. J. Snaith, R. Zhu and Q. Gong, *Adv. Funct. Mater.*, 2016, **26**, 3508–3514.
38 Z. Wang, J. Jin, Y. Zheng, X. Zhang, Z. Zhu, Y. Zhou, X. Cui, J. Li, M. Shang, X. Zhao, S. Liu and Q. Tai, *Adv. Energy Mater.*, 2021, **11**, 2102169.
39 D. Luo, L. Zhao, J. Wu, Q. Hu, Y. Zhang, Z. Xu, Y. Liu, T. Liu, K. Chen, W. Yang, W. Zhang, R. Zhu and Q. Gong, *Adv. Mater.*, 2017, **29**, 1604758.
40 Q. Niu, H. Lv, X. Duan, M. Jiang, Y. Zhang, Z. Wang, J. Tong, Y. Deng, Y. Ma, H. Zhang, R. Xia, W. Zeng and Y. Min, *Synth. Met.*, 2019, **254**, 85–91.
41 J. Zhao, S. O. Fürer, D. P. McMeekin, Q. Lin, P. Lv, J. Ma, W. L. Tan, C. Wang, B. Tan, A. S. R. Chesman, H. Yin, A. D. Scully, C. R. McNeill, W. Mao, J. Lu, Y. B. Cheng and U. Bach, *Energy Environ. Sci.*, 2022, **16**, 138–147.
42 G. Tang, P. You, Q. Tai, R. Wu and F. Yan, *Sol. RRL*, 2018, **2**, 1800066.
43 J. Xi, H. Wang, J. Yuan, X. Yan, P. Siffalovic and J. Tian, *Sol. RRL*, 2021, **5**, 2100747.
44 Z. Zeng, J. Zhang, X. Gan, H. Sun, M. Shang, D. Hou, C. Lu, R. Chen, Y. Zhu and L. Han, *Adv. Energy Mater.*, 2018, **8**, 1801050.
45 X. Xu, H. Zhang, E. Li, P. Ru, H. Chen, Z. Chen, Y. Wu, H. Tian and W. H. Zhu, *Chem. Sci.*, 2020, **11**, 3132–3140.
46 S. Kajal, G. H. Kim, C. W. Myung, Y. S. Shin, J. Kim, J. Jeong, A. Jana, J. Y. Kim and K. S. Kim, *J. Mater. Chem. A*, 2019, **7**, 21740–21746.
47 R. Kottokkaran, H. A. Gaonkar, B. Bagheri and V. L. Dalal, *J. Vac. Sci. Technol., A*, 2018, **36**, 041201.
48 J. A. Aguiar, S. Wozny, T. G. Holesinger, T. Aoki, M. K. Patel, M. Yang, J. J. Berry, M. Al-Jassim, W. Zhou and K. Zhu, *Energy Environ. Sci.*, 2016, **9**, 2372–2382.
49 J. Cao, X. Jing, J. Yan, C. Hu, R. Chen, J. Yin, J. Li and N. Zheng, *J. Am. Chem. Soc.*, 2016, **138**, 9919–9926.
50 W. S. Yang, J. H. Noh, N. J. Jeon, Y. C. Kim, S. Ryu, J. Seo and S. Il Seok, *Science*, 2015, **348**, 1234–1237.
51 *Org. Synth.*, 1990, **69**, 31.
52 B. Zhao, S. F. Jin, S. Huang, N. Liu, J. Y. Ma, D. J. Xue, Q. Han, J. Ding, Q. Q. Ge, Y. Feng and J. S. Hu, *J. Am. Chem. Soc.*, 2018, **140**, 11716–11725.
53 Q. Ye, F. Ma, Y. Zhao, S. Yu, Z. Chu, P. Gao, X. Zhang and J. You, *Small*, 2020, **16**, 2005246.
54 K. P. Goetz, A. D. Taylor, F. Paulus and Y. Vaynzof, *Adv. Funct. Mater.*, 2020, **30**, 1910004.
55 L. Wang, C. McCleese, A. Kovalsky, Y. Zhao and C. Burda, *J. Am. Chem. Soc.*, 2014, **136**, 12205–12208.
56 S. Tan, T. Huang, I. Yavuz, R. Wang, T. W. Yoon, M. Xu, Q. Xing, K. Park, D. K. Lee, C. H. Chen, R. Zheng, T. Yoon, Y. Zhao, H. C. Wang, D. Meng, J. Xue, Y. J. Song, X. Pan, N. G. Park, J. W. Lee and Y. Yang, *Nature*, 2022, **605**, 268–273.
57 R. Ji, Z. Zhang, Y. J. Hofstetter, R. Buschbeck, C. Hänisch, F. Paulus and Y. Vaynzof, *Nat. Energy*, 2022, **7**, 1170–1179.
58 C. Zheng, A. Liu, C. Bi and J. Tian, *Wuli Huaxue Xuebao*, 2021, **37**, 2007084.
59 C. Bi, S. Wang, S. V. Kershaw, K. Zheng, T. Pullerits, S. Gaponenko, J. Tian and A. L. Rogach, *Adv. Sci.*, 2019, **6**, 1900462.
60 F. Liu, Y. Zhang, C. Ding, S. Kobayashi, T. Izuishi, N. Nakazawa, T. Toyoda, T. Ohta, S. Hayase, T. Minemoto,

K. Yoshino, S. Dai and Q. Shen, *ACS Nano*, 2017, **11**, 10373–10383.
61 N. J. Podraza, B. Subedi, C. Li, C. Chen, D. Liu, M. M. Junda, Z. Song and Y. Yan, *ACS Appl. Mater. Interfaces*, 2022, **14**, 7796–7804.
62 H. Mehdizadeh-Rad and J. Singh, *ChemPhysChem*, 2019, **20**, 2712–2717.
63 D. Becker-Koch, B. Rivkin, F. Paulus, H. Xiang, Y. Dong, Z. Chen, A. A. Bakulin and Y. Vaynzof, *J. Phys.: Condens. Matter*, 2019, **31**, 124001.
64 Q. Jiang, Z. Chu, P. Wang, X. Yang, H. Liu, Y. Wang, Z. Yin, J. Wu, X. Zhang and J. You, *Adv. Mater.*, 2017, **29**, 1703852.
65 T. J. Jacobsson, J. P. Correa-Baena, E. Halvani Anaraki, B. Philippe, S. D. Stranks, M. E. F. Bouduban, W. Tress, K. Schenk, J. Teuscher, J. E. Moser, H. Rensmo and A. Hagfeldt, *J. Am. Chem. Soc.*, 2016, **138**, 10331–10343.
66 T. Abzieher, T. Feeney, F. Schackmar, Y. J. Donie, I. M. Hossain, J. A. Schwenzer, T. Hellmann, T. Mayer, M. Powalla and U. W. Paetzold, *Adv. Funct. Mater.*, 2021, **31**, 2104482.
67 M. Roß, L. Gil-Escrig, A. Al-Ashouri, P. Tockhorn, M. Jošt, B. Rech and S. Albrecht, *ACS Appl. Mater. Interfaces*, 2020, **12**, 39261–39272.
68 S. Bitton, Q. An, Y. Vaynzof and N. Tessler, *ACS Appl. Energy Mater.*, 2021, **4**, 8709–8714.
69 C. Bi, Q. Wang, Y. Shao, Y. Yuan, Z. Xiao and J. Huang, *Nat. Commun.*, 2015, **6**, 7747.
70 L. Mao, T. Yang, H. Zhang, J. Shi, Y. Hu, P. Zeng, F. Li, J. Gong, X. Fang, Y. Sun, X. Liu, J. Du, A. Han, L. Zhang, W. Liu, F. Meng, X. Cui, Z. Liu and M. Liu, *Adv. Mater.*, 2022, **34**, 2206193.
71 H. Eggers, F. Schackmar, T. Abzieher, Q. Sun, U. Lemmer, Y. Vaynzof, B. S. Richards, G. Hernandez-Sosa and U. W. Paetzold, *Adv. Energy Mater.*, 2020, **10**, 1903184.
72 Q. An, F. Paulus and Y. Vaynzof, *ACS Appl. Energy Mater.*, 2021, **4**, 2990–2998.
73 A. R. M. Alghamdi, M. Yanagida, Y. Shirai, G. G. Andersson and K. Miyano, *ACS Omega*, 2022, **7**, 12147–12157.
74 M. I. Haider, A. Fakhruddin, S. Ahmed, M. Sultan and L. Schmidt-Mende, *Sol. Energy*, 2022, **233**, 326–336.
75 N. Tessler and Y. Vaynzof, *ACS Energy Lett.*, 2020, **5**, 1260–1270.
76 W. Chen, F. Z. Liu, X. Y. Feng, A. B. Djurišić, W. K. Chan and Z. B. He, *Adv. Energy Mater.*, 2017, **7**, 1700722.
77 W. Chen, Y. Wu, J. Fan, A. B. Djurišić, F. Liu, H. W. Tam, A. Ng, C. Surya, W. K. Chan, D. Wang and Z. B. He, *Adv. Energy Mater.*, 2018, **8**, 1703519.
78 W. Chen, Y. Zhou, L. Wang, Y. Wu, B. Tu, B. Yu, F. Liu, H.-W. Tam, G. Wang, A. B. Djurišic, L. Huang and Z. He, *Adv. Mater.*, 2018, **30**, 1800515.
79 M. Degani, Q. An, M. Albaladejo-Siguan, Y. J. Hofstetter, C. Cho, F. Paulus, G. Grancini and Y. Vaynzof, *Sci. Adv.*, 2021, **7**, 7930.
80 Q. Wang, B. Chen, Y. Liu, Y. Deng, Y. Bai, Q. Dong and J. Huang, *Energy Environ. Sci.*, 2017, **10**, 516–522.
81 Q. Sun, P. Fassl, D. Becker-Koch, A. Bausch, B. Rivkin, S. Bai, P. E. Hopkinson, H. J. Snaith and Y. Vaynzof, *Adv. Energy Mater.*, 2017, **7**, 1700977.
82 Z. Zhang, Y. Zhou, Y. Cai, H. Liu, Q. Qin, X. Lu, X. Gao, L. Shui, S. Wu and J. M. Liu, *J. Power Sources*, 2018, **377**, 52–58.
83 J. Sun, K. Ma, Z. Lin, Y. Tang, D. Varadharajan, A. X. Chen, H. R. Atapattu, Y. H. Lee, K. Chen, B. W. Boudouris, K. R. Graham, D. J. Lipomi, J. Mei, B. M. Savoie and L. Dou, *Adv. Mater.*, 2023, 2300647.
84 J. A. Kress, C. Quarti, Q. An, S. Bitton, N. Tessler, D. Beljonne and Y. Vaynzof, *ACS Energy Lett.*, 2022, **7**, 3302–3310.
85 A. A. Sutanto, P. Caprioglio, N. Drigo, Y. J. Hofstetter, I. Garcia-Benito, V. I. E. Queloz, D. Neher, M. K. Nazeeruddin, M. Stolterfoht, Y. Vaynzof and G. Grancini, *Chem*, 2021, **7**, 1903–1916.
86 V. Lami, A. Weu, J. Zhang, Y. Chen, Z. Fei, M. Heeney, R. H. Friend and Y. Vaynzof, *Joule*, 2019, **3**, 2513–2534.